Geophysical Journal International

Geophys. J. Int. (2015) **203,** 1072–1084 doi: 10.1093/gji/ggv331

GJI Geomagnetism, rock magnetism and palaeomagnetism

The electrical conductivity of CO_2-bearing pore waters at elevated pressure and temperature: a laboratory study and its implications in CO_2 storage monitoring and leakage detection

Jana H. Börner,[1] Volker Herdegen,[2] Jens-Uwe Repke[2] and Klaus Spitzer[1]

[1]*Institute of Geophysics and Geoinformatics, Technical University Bergakademie Freiberg, Germany. E-mail: jana.boerner@geophysik.tu-freiberg.de*

[2]*Institute of Thermal, Environmental and Natural Products Process Engineering, Technical University Bergakademie Freiberg, Germany*

Accepted 2015 August 7. Received 2015 July 31; in original form 2015 June 5

SUMMARY

The electrical rock conductivity is a sensitive indicator for carbon dioxide (CO_2) injection and migration processes. For a reliable balancing of the free CO_2 in pore space with petrophysical models such as Archie's law or for the detection of migrating CO_2, detailed knowledge of the pore water conductivity during interaction with CO_2 is essential but not available yet. Contrary to common assumptions, pore water conductivity cannot be assumed constant since CO_2 is a reactive gas that dissolves into the pore water in large amounts and provides additional charge carriers due to the dissociation of carbonic acid. We consequently carried out systematic laboratory experiments to quantify and analyse the changes in saline pore water conductivity caused by CO_2 at thermodynamic equilibrium. Electrical conductivity is measured on pore water samples for pressures up to 30 MPa and temperatures up to 80 °C. The parameter range covers the gaseous, liquid and supercritical state of the CO_2 involved. Pore water salinities from 0.006 up to 57.27 g L^{-1} sodium chloride were investigated as well as selective other ion species. At the same time, the CO_2 concentration in the salt solution was determined by a wet-chemical procedure. A two-regime behaviour appears: for small salinities, we observe an increase of up to more than factor 3 in the electrical pore water conductivity, which strongly depends on the solution salinity (low-salinity regime). This is an expected behaviour, since the additional ions originating from the dissociation of carbonic acid positively contribute to the solution conductivity. However, when increasing salinities are considered this effect is completely diminished. For highly saline solutions, the increased mutual impeding causes the mobility of all ions to decrease, which may result in a significant reduction of conductivity by up to 15 per cent despite the added CO_2 (high-salinity regime). We present the data set covering the pressure, temperature, salinity and ion species dependence of the CO_2 effect. Furthermore, the observations are analysed and predicted with a semi-analytical formulation for the electrical pore water conductivity taking into account the species' interactions. For the applicability of our results in practice of exploration and monitoring, we additionally provide a purely empirical formulation to compute the impact of CO_2 on pore water conductivity at equilibrium which only requires the input of pressure, temperature and salinity information.

Key words: Electrical properties; High-pressure behaviour.

1 INTRODUCTION

The electrical conductivity of porous rocks has long been of great interest in geophysical research and exploration. It has been acknowledged that electrical rock properties give access to reservoir properties as well as the processes in pore space due to their sensitivity to conductive pore fluids (Archie 1942). The resulting impact of the presence of non-conducting fluids such as oil or natural gas, which reduce the fraction of conducting saline pore water, is widely used in hydrocarbon exploration and has been subject to numerous petrophysical studies and models (e.g. Archie 1942; Waxman & Smits 1968; Vinegar & Waxman 1984). The models turned out to be valid for rock matrix / pore water / air systems as well and are applied to date in deep exploration as well as in investigations of the vadose zone (e.g. Binley *et al.* 2002; Dell'Aversana *et al.* 2011). Archie's law has been extended to cover multiple rock types, pore space geometries and phases of varying conductivity, respectively (e.g. Glover 2010; Müller-Huber *et al.* 2015).

Table 1. Overview of all quantities, parameters and constants used in this study in alphabetical order.

Symbol	Explanation	Unit
a	Activity	g L^{-1}
$\mathring{a}$	Distance of closest approach	m
b	Molality	mol kg^{-1}
c	Concentration	g L^{-1}
d	Density	kg L^{-1}
D	Diffusion coefficient	m^2 s^{-1}
e	Elementary charge	C
F_c	Faraday's constant	C mol^{-1}
g	Interaction parameter (eqs 23 and 24)	L g^{-1}
h	Interaction parameter (eqs 23 and 24)	L^2 g^{-2}
I	True ionic strength	mol L^{-1}
K	Equilibrium constant	g L^{-1}
m	Cementation exponent (Archie 1942)	–
M	Molar mass	g mol^{-1}
n	Saturation exponent (Archie 1942)	–
N_A	Avogadro constant	mol^{-1}
p	Pressure	MPa
q	Empirical parameter (eq. 25)	varying
R	Universal gas constant	J mol^{-1} K^{-1}
S	Saturation	–
T	Temperature	K or °C
z	Charge number	–
α	Degree of dissociation	–
γ	Activity coefficient	–
ϵ	Permittivity	F m^{-1}
κ	Reciprocal of the Debye length	m^{-1}
Λ	Limiting molar conductivity	S L m^{-1} g^{-1}
ρ_w	Electrical pore water resistivity	Ωm
σ	Electrical rock conductivity	S m^{-1}
σ_w	Pore water conductivity	S m^{-1}
σ_w^{norm}	Conductivity contrast	–
Φ	Porosity	–

All approaches have in common that during observation no interaction between the fluid phases is assumed. For example, Archie's law states for the electrical conductivity σ of clay-free porous rocks:

$$\sigma = S_w^n \Phi^m \sigma_w \tag{1}$$

Here, S_w denotes pore water saturation, Φ is porosity, n is the saturation exponent, and m is the cementation exponent (see also Table 1). The electrical conductivity of the pore water σ_w hereby depends on the concentration of dissolved salts c_{salt} and temperature T:

$$\sigma_w = f(c_{salt}, T). \tag{2}$$

However, when a reactive gas such as carbon dioxide (CO_2) enters the pore space of a formerly undisturbed two-phase system of mineral matrix and pore water, this assumption can definitely not be maintained (Fig. 1). It is well known that CO_2 sequestration gives rise to many geochemical processes, which change fluids and grain surfaces (e.g. Wigand *et al.* 2008; Kummerow & Spangenberg 2011; Börner *et al.* 2013). Due to the sensitivity to pore fluids, geoelectrical techniques have been applied for the monitoring of CO_2 storage formations (e.g. Kiessling *et al.* 2010; Vilamajó *et al.* 2013). Indeed, a free CO_2 phase acts as an electrical insulator, but when in contact with an aqueous phase it dissolves in it in large amounts and changes its properties. Consequently additional quantities like pressure p and the dissolved CO_2 influence the pore water conductivity:

$$\sigma_w = f(c_{salt}, T, p, c_{CO_2}). \tag{3}$$

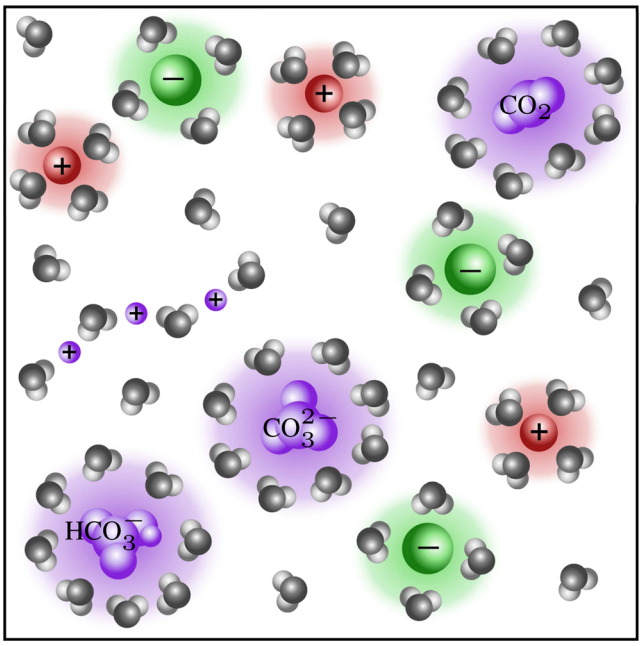

Figure 1. Schematic molecular representation of a CO_2-bearing pore water. The pore water (grey) contains cations (red) and anions (green) of dissociated salts and additional charged and neutral species originating from CO_2dissolution and partial dissociation (purple).

These effects have been reported by Börner *et al.* (2013) and an empirical adaptation of Archie's law has been proposed to consider the dissolved CO_2. However, the formulation is restricted, for example, to pressures up to 9 MPa and 25 °C. This former study motivated a systematic investigation of the impact of CO_2 on pore water as a separate phase in order to cover a wide range of depths and geological environments and to reveal the relevant phenomena.

Carbon dioxide capture and storage (CCS) is one field of application for the results of the presented study. CO_2 reaches the supercritical state at about 800 m depth making CCS feasible below (IPCC 2005). Operational sites utilize reservoirs ranging from little below 800 m (e.g. Sleipner, Norway) down to 2000 m and more (e.g. Otway, Australia). Besides structural trapping mechanisms, which may be covered with Archie's law, the trapping by dissolution in the formation water is a central part of the geotechnology (Hitchon 1996). Geophysical methods are widely used and developed as monitoring techniques for both the storage reservoirs and the near-surface areas for leakage detection. Consequently, knowledge about the pore water conductivity is essential, when the saturation of a free CO_2 phase in a reservoir is supposed to be estimated with petrophysical models or when potential leakage areas are monitored.

We therefore present an extensive laboratory study of the electrical conductivity of salt solutions with CO_2 in equilibrium at numerous pressures (1–30 MPa), temperatures (8–80 °C) and salinities (0.006–57.27 g L^{-1}). The selected temperature and pressure levels, ion species and salinities cover all states of aggregation of CO_2 (except solid state) and represent different geological environments down to 3000 m depth (estimated with a geothermal gradient of 3 K/100 m and water column pressure as pore pressure). The salinity of pore waters in natural environments varies strongly. Low salinities of 0.05–0.2 g L^{-1} may be found in clean fresh water aquifers (Kunkel *et al.* 2002), whereas salinity generally increases with depth due to increased solubility at elevated pressure (e.g. Möller *et al.* 1997; Meju 2002). Salinity may easily exceed sea-water salinity

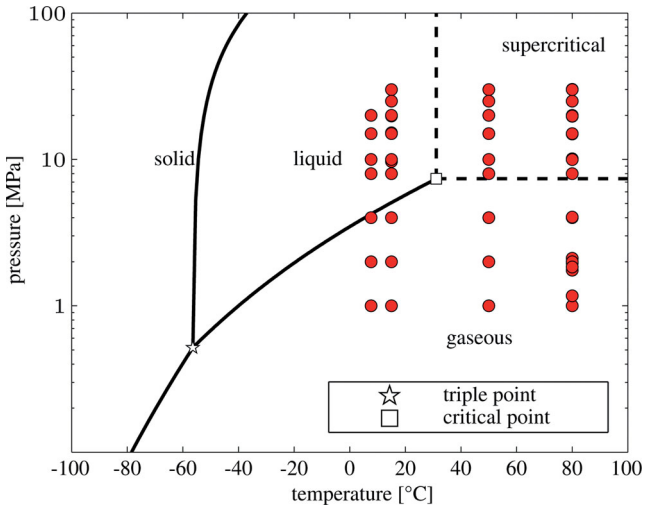

Figure 2. Phase diagram of CO_2 after Span & Wagner (1996) and overview of pressure and temperature conditions investigated in the study here (red dots). Note, that numerous p–T conditions were accessed for multiple salinities and/or salt species.

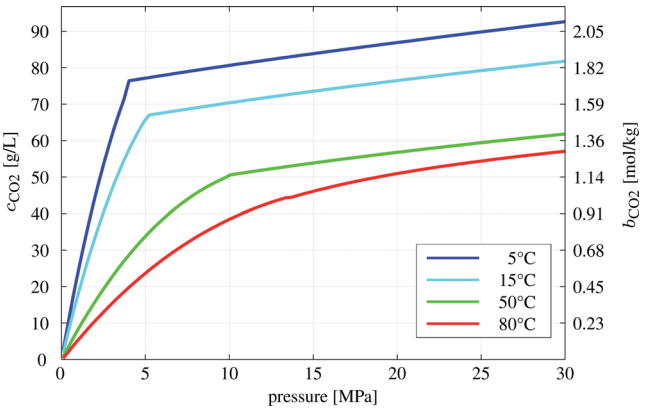

Figure 3. Solubility of carbon dioxide in pure water at thermodynamic equilibrium in terms of both concentration (left axis) and molality (right axis) after Duan *et al.* (2006) for several temperatures. The sharp bend at subcritical temperatures is caused by the phase transition from gaseous to liquid state (*cf.* Fig. 2).

(approximately 30 g L^{-1}) at great depths (e.g. Yardley *et al.* 2011). The investigated conditions contain implications for a wide variety of applications, therefore:

(i) Low pressures, temperatures and salinities may be found in shallow aquifers, which might be monitored for leakage detection.
(ii) High pressures, temperatures and salinities may be found in deep aquifers, which might host a CO_2 storage.

Apart from the conductivity increasing behaviour at low salinities reported by Börner *et al.* (2013), we observe a significant decrease of conductivity at high salinities. Hence, we differentiate between a low- and a high-salinity regime. We deduce a semi-analytical model for the conductivity change, which explains and predicts our observations. In order to make our results easy to use, we additionally provide a purely empirical formulation, which solely requires the input of pressure, temperature and salinity.

2 THEORY

2.1 Dissolution and dissociation of CO_2

CO_2 is a colourless, odourless, non-toxic but asphyxiant substance, which is gaseous at normal conditions (25 °C, 0.1 MPa). CO_2 reaches the supercritical state at moderate conditions of 30.98 °C and 7.377 MPa (see phase diagram in Fig. 2; Span & Wagner 1996). At supercritical state, which is reached at approximately 800 m depth below the Earth's surface, the fluid-like density and gas-like viscosity of CO_2 facilitate the geotechnology of CO_2 storage (IPCC 2005; Marini 2007).

The amount of CO_2, which is dissolved in a pore water with known sodium chloride (NaCl) content at thermodynamic equilibrium, is a function of pressure p, temperature T and salinity b_{NaCl}:

$$b_{CO_2} = f(p, T, b_{NaCl}), \tag{4}$$

where b_i denotes molality and is in mol kg^{-1}. In this study, the solubility b_{CO_2} is computed with the approach presented by Duan *et al.* (2006) and cross-checked by chemical analysis. Fig. 3 shows the pressure-dependent solubility of CO_2 in pure water for several temperatures. At low temperatures, a sharp bend is evident at the phase change from gaseous to liquid state.

For most of the following considerations, it is convenient to formulate in terms of concentration rather than molality. Molality, which includes reference to the mass of solvent, may be transformed into concentration c, which is formulated with reference to the solution volume by

$$c_i(p, T, b_{1\ldots n}) = b_i M_i \frac{d(p, T, b_{1\ldots n})}{1 + \sum_{j=1}^{n}(0.001 \cdot b_j M_j)}, \tag{5}$$

where c_i is in g L^{-1}, M_i is the molar mass of solute i, d is the density of the solution in kg L^{-1}, M_j is the molar mass of solute j in g mol^{-1} and n is the number of solutes. Note that c_i depends on the molality of all other compounds and on both temperature and pressure (due to the p and T dependence of the solution density d). Duan *et al.* (2008) provide a model for the density of the ternary system CO_2–NaCl–H_2O, which was used for the computation of solution densities in this study. In order to keep comparability, all initial solution properties are documented at ambient pressure and 25 °C.

The dissolved $CO_{2(aq)}$ (c_{CO_2}) forms uncharged aqueous complexes (e.g. Li & Duan 2007). A fraction of this $CO_{2(aq)}$ reacts with the pore water to form carbonic acid H_2CO_3. The carbonic acid is unstable and dissociates in two steps into protons, hydrocarbonate and carbonate ions (Fig. 1). Consequently, the summarized dissociation equations read:

$$CO_{2(aq)} + H_2O \overset{K_1}{\rightleftharpoons} H^+ + HCO_3^- \tag{6}$$

$$HCO_3^- \overset{K_2}{\rightleftharpoons} H^+ + CO_3^{2-}. \tag{7}$$

These electrically charged species occur in addition to the H^+ and OH^- ions of the self dissociation of water and anions and cations of dissolved salts.

The concentrations of the charged species at chemical equilibrium are governed by the equilibrium constants K_1 and K_2 (in g L^{-1}, referring to eqs 6 and 7), respectively, which are also pressure, temperature and salinity dependent:

$$K_1, K_2 = f(p, T, c_{NaCl}). \tag{8}$$

We calculate them by combining the approaches given by Li & Duan (2007) and Millero *et al.* (2007) (see also Börner *et al.* 2013).

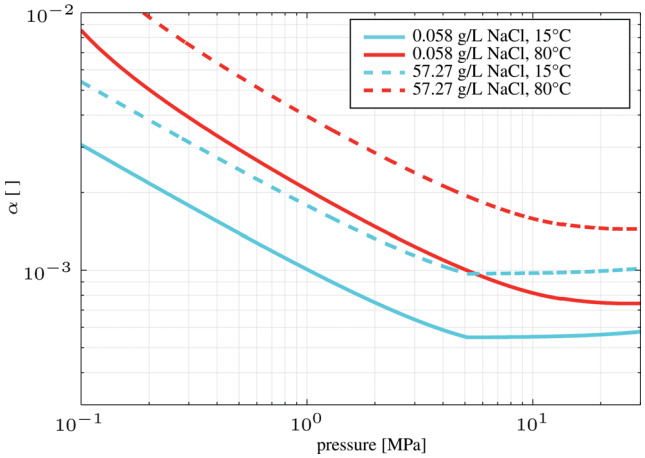

Figure 4. Degree of dissociation of carbonic acid according to eq. (9) for two salinities at two temperatures. The sharp bend at 15 °C is caused by the phase transition from gaseous to liquid state (*cf.* Fig. 2).

K_1 exceeds K_2 by several orders of magnitude. Therefore, we can restrict our considerations to the first stage of dissociation. With the help of the dissociation constant we can calculate the dimensionless degree of dissociation α, which describes the fraction of the dissolved CO_2 actually forming charge carriers and lies between 0 (no dissociation) and 1 (fully dissociated). We do this by applying Ostwald's dilution law (e.g. Robinson & Stokes 2002). The dilution law is valid up to approximately 0.01 mol kg^{-1}. Inaccuracies might be caused by this simplified approach when high concentrations are considered. For weak acids—such as the carbonic acid—and small degrees of dissociation $\alpha \ll 1$, Ostwald's law reads:

$$\alpha = \sqrt{\frac{K_1}{c_{CO_2}}}. \tag{9}$$

Fig. 4 shows the degree of dissociation of carbonic acid in 0.058 (i.e. 0.001 mol kg^{-1}, straight line) and 57.27 g L^{-1} NaCl (i.e. 1 mol kg^{-1}, dashed line) solutions versus pressure at 15 (cyan) and 80 °C (red). The diagram demonstrates the generally very low degree of dissociation. α is largest for low pressures, high salinities and high temperatures and shows a characteristic change in trend above approximately 5 MPa. Based on the concentration of dissolved carbon dioxide c_{CO_2} and the degree of dissociation, the concentrations of the dissociated carbon dioxide $c_{CO_{2(dis)}}$ and of the remaining, electrically neutral carbon dioxide $c_{CO_{2(aq)}}$ can be derived as

$$c_{CO_{2(dis)}} = \alpha c_{CO_2} \tag{10}$$

$$c_{CO_{2(aq)}} = (1-\alpha) c_{CO_2}. \tag{11}$$

2.2 Electrical conductivity of aqueous solutions

The contribution $\sigma_{w,i}$, which a charged chemical species i makes to the conductivity of an aqueous solution (the pore water) at infinite dilution is described by the Nernst–Einstein relation (e.g. Robinson & Stokes 2002):

$$\sigma_{w,i} = \frac{z_i^2 F_c^2}{RTM_i} D_i c_i, \tag{12}$$

where D_i denotes the diffusion coefficient, z_i the species' charge number, R the universal gas constant, T absolute temperature and F_c Faraday's constant. The species and environment-dependent quantities are subsumed as limiting molar conductivity Λ_i, which bears the unit S L m^{-1} g^{-1}. Therefore,

$$\sigma_{w,i} = \Lambda_i c_i. \tag{13}$$

The limiting molar conductivity determines the electrical conductivity at infinite dilution and is a temperature-dependent constant. For example, Λ_{NaCl} is 0.216 S L m^{-1} g^{-1} at 25 °C. The electrical conductivity of the aqueous solution σ_w is the sum of all contributions:

$$\sigma_w = \sum_{i=1}^{k} [\Lambda_i c_i]. \tag{14}$$

Due to the large amount of NaCl and CO_2 dissolved in the saline solution, the latter cannot be assumed to be infinitely diluted any more. The ions interfere with one another and their ability to contribute to the electrolytical conductivity decreases. The activity a_i of a chemical species is the effective concentration of that species and is defined as:

$$a_i = \gamma_i c_i, \tag{15}$$

where γ_i is the dimensionless activity coefficient. For ideal and infinitely diluted solutions γ_i equals 1. Theoretically, each ion in an aqueous solution has an activity of its own. Since single-species activities cannot be measured, it is useful to work with the average activity of a chemical compound (e.g. Hamann & Vielstich 1998). Now we can express eq. (14) in terms of activities:

$$\sigma_w = \sum_{i=1}^{k} [\Lambda_i a_i] = \sum_{i=1}^{k} [\Lambda_i \gamma_i c_i]. \tag{16}$$

The classic Debye–Hückel-theory deduced the average activity coefficient of a diluted solution of compound i (Debye 1923; Debye & Hückel 1923a,b). For readability reasons, activity coefficients, which are basically exponential functions ($\gamma_i = e^{-x}$ with x being a function of many dependencies), are usually given in their logarithmized form ($\ln(\gamma_i) = -x$):

$$\ln(\gamma_i) = -\frac{|z_+ z_-| e^2 N_A}{2\epsilon RT} \frac{\kappa}{1 + \mathring{a}\kappa} \tag{17}$$

Here, z_+ and z_- are the charge numbers of the cation and anion originating from the dissociation of compound i, e is the elementary electric charge, N_A is the Avogadro constant and ϵ is solution permittivity. $\mathring{a}$ in eq. (17) is the so-called 'distance of closest approach', which represents the radius of the ion cloud (Helgeson 1969; Hamann & Vielstich 1998). In accordance with Helgeson (1969), it is set to be 4.2×10^{-10} m in this case. The parameter κ is the reciprocal of the Debye length and is in units of m^{-1}, therefore:

$$\kappa = \sqrt{\frac{8\pi e^2 N_A^2}{1000 \epsilon RT} I}, \tag{18}$$

where I is the true ionic strength, which is defined as:

$$I = \frac{1}{2} \sum_{j=1}^{n} \frac{\alpha_j c_j z_j^2}{M_j} \tag{19}$$

with n being the number of ion species. For example, a pure NaCl solution contains Na^+ and Cl^- ions, therefore $n = 2$. Consequently, I bears the unit mol L^{-1}. For fully dissociated ($\alpha = 1$) 1:1-electrolytes (such as NaCl), I equals to the solution's molar concentration. Numerous extensions and adaptations of the Debye–Hückel activity coefficient have been developed to account for the highly individual and complicated behaviour of chemical species at high

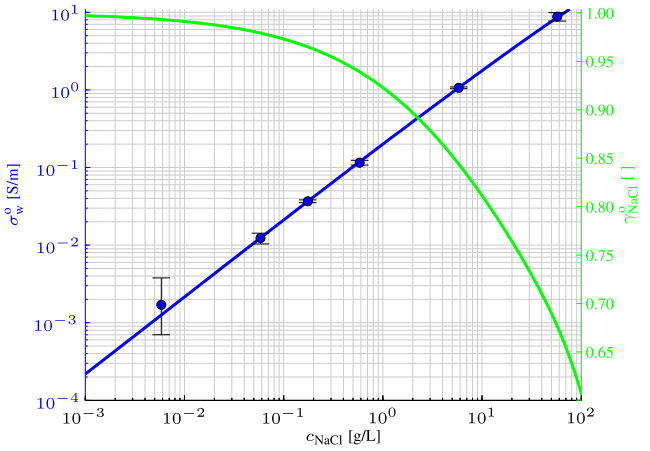

Figure 5. Properties of aqueous NaCl solutions: electrical conductivity (blue line, based on data from Hamann & Vielstich 1998); activity coefficient γ^o_{NaCl} derived from eq. (16) (green line, $\Lambda_{NaCl} = 0.216$ S L m^{-1} g^{-1} at 25 °C). Blue circles denote the conductivity of the NaCl solutions for the supposed concentrations used in this study (*cf.* Table 2). The error bars show the threefold standard deviation of initial solution conductivity (determined by repeated manufacturing).

ionic strengths (e.g. Guggenheim & Turgeon 1955; Davies 1962; Bromley 1973; Pitzer 1991).

Building on the presented theoretical considerations the experimental details of the conducted measurements are explained in the following section. First, the sample pore waters and their properties are introduced, than the experimental setup and procedures are described.

3 MATERIAL AND METHODS

3.1 Salt solutions and CO_2

For all experiments presented in this study, the initial solutions were set up in terms of molality b_i due to the simple procedure. A distinct amount of salt was weighed out and added to a known mass of deionized water. Since the dependence of pore water conductivity σ_w on concentration is well known for sodium chloride (*cf.* Fig. 5), the solution properties could be cross-checked by measuring conductivity in the case of NaCl. The properties of pure NaCl solutions known from the literature (e.g. Hamann & Vielstich 1998) are plotted in Fig. 5, where the straight blue line represents the solution conductivity. The limiting molar conductivity is also well documented ($\Lambda_{NaCl} = 0.216$ S L m^{-1} g^{-1} at 25 °C). Consequently, we can calculate the activity coefficient of pure NaCl solutions γ^o_{NaCl} with eq. (16) (see green line in Fig. 5).

The NaCl solutions used in this study and their measured conductivities are plotted in Fig. 5, as well (blue circles). The solutions set up for our experiments coincide very well with the supposed properties. At very low concentrations the observed variation is large. This is due to the very small mass of salt, which has to be weighed out (*cf.* Table 2). Results at this concentration have to be interpreted with great care, therefore.

To exemplarily evaluate the influence of the ion species on conductivity, potassium chloride (KCl), magnesium sulphate ($MgSO_4$) and magnesium chloride ($MgCl_2$) solutions were investigated, as well (*cf.* Table 2). All aqueous solutions were exposed to 99.5 per cent pure CO_2 at different pressures and temperatures.

Table 2. Properties of the salt solutions used in this study (see also Fig. 5). b_i denotes molality, c_i concentration, σ^o_w conductivity and $\rho^o_w = \frac{1}{\sigma^o_w}$ electrical resistivity.

Salt	b_i [mol kg^{-1}]	c_i [g L^{-1}]	σ^o_w at 25 °C [S m^{-1}]	ρ^o_w at 25 °C [Ωm]
NaCl	0.0001	0.006	0.0017	585
NaCl	0.001	0.058	0.0123	81.5
NaCl	0.003	0.175	0.0368	27.2
NaCl	0.01	0.582	0.1155	8.66
NaCl	0.1	5.817	1.0639	0.94
NaCl	1	57.27	8.7999	0.11
KCl	0.01	0.746	0.1415	7.07
$MgSO_4$	0.01	1.204	0.1455	6.87
$MgCl_2$	0.01	0.952	0.2208	4.53

3.2 Experimental setup

All experiments presented in this study were carried out with an experimental setup outlined in Fig. 6. The apparatus is based on the setup of Börner *et al.* (2013). A hot air cabinet and a two-staged feed pressure regulation has been added to improve the stability of the operating conditions and the accuracy of the conductivity measurements. Additionally, it contains a sampling system to provide concentration measurements of dissolved CO_2 with a wet chemical analysis method.

The autoclave is capable to produce maximum pressures of 40 MPa at a maximum temperature of 80 °C. The core of the experimental setup is the measuring cell of ca. 0.75 L volume placed inside of the autoclave shown in Fig. 7. The main challenge for the design of the cell is to withstand temperature and CO_2 exposure during the experiments.

Therefore, the measuring cell completely consists of glass and all electrodes are made of platinum to avoid any electrochemical reaction with the brines on the material surface throughout the course of the experiment. Six wire rings 0.5 mm in diameter serve as potential electrodes. Wire mesh current electrodes were placed at the top and bottom of the measuring cell. To ensure electrical contact of the current mesh at the top, a polytetrafluoroethylene (PTFE) mount is installed also attaching a PTFE coated resistance thermometer Pt 100 (accuracy: ±0.16 °C at 5 °C and ±0.31 °C at 80 °C) and a thin plastic sample capillary. The pressure is measured with an accuracy of ±0.1 MPa in the operating range (corresponds to 0.25 per cent of the measuring span). To insure that the electrical measurement remains unperturbed by the fluid sampling process an excess pore water volume is provided. The inevitable holes in the glass for the electrode cables were closed by a suitable two component adhesive.

For the concentration measurement, a 1 mL sample of CO_2 saturated brine can be extracted from the autoclave through the capillary during operation. The CO_2 dissolved in the sample is determined later on by precipitation in a barium hydroxide solution and back titration.

3.3 Experimental procedure

For the electrical conductivity determination at equilibrium state, the measuring cell (*cf.* Fig. 7) is filled with a brine solution, for example, a sodium chloride solution of known temperature, salinity, and conductivity σ^o_w until the upper current electrode is fully covered by approximately 2 cm of the solution. This excess fluid allows for sampling during the experiment without influencing the measured solution conductivity.

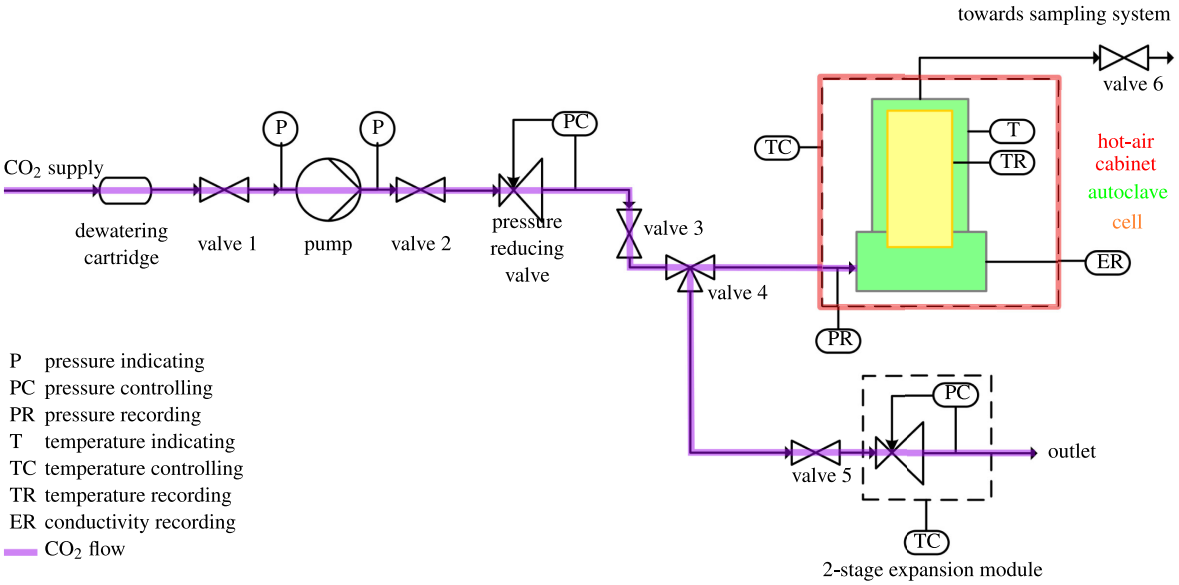

Figure 6. Scheme of the laboratory setup used for the experiments.

Temperature, pressure and conductivity are indicated and monitored throughout the whole experiment. Vertical conductivity gradients relating to concentration gradients may be determined by measuring the electric potential difference at different locations along the sample. For diffusion-dominated equilibration, this allows for following the dissolution speed or the transport resistance of the CO_2 into the brine solution over the cell height. It turned out that density gradients originating from CO_2 dissolution (CO_2-rich pore

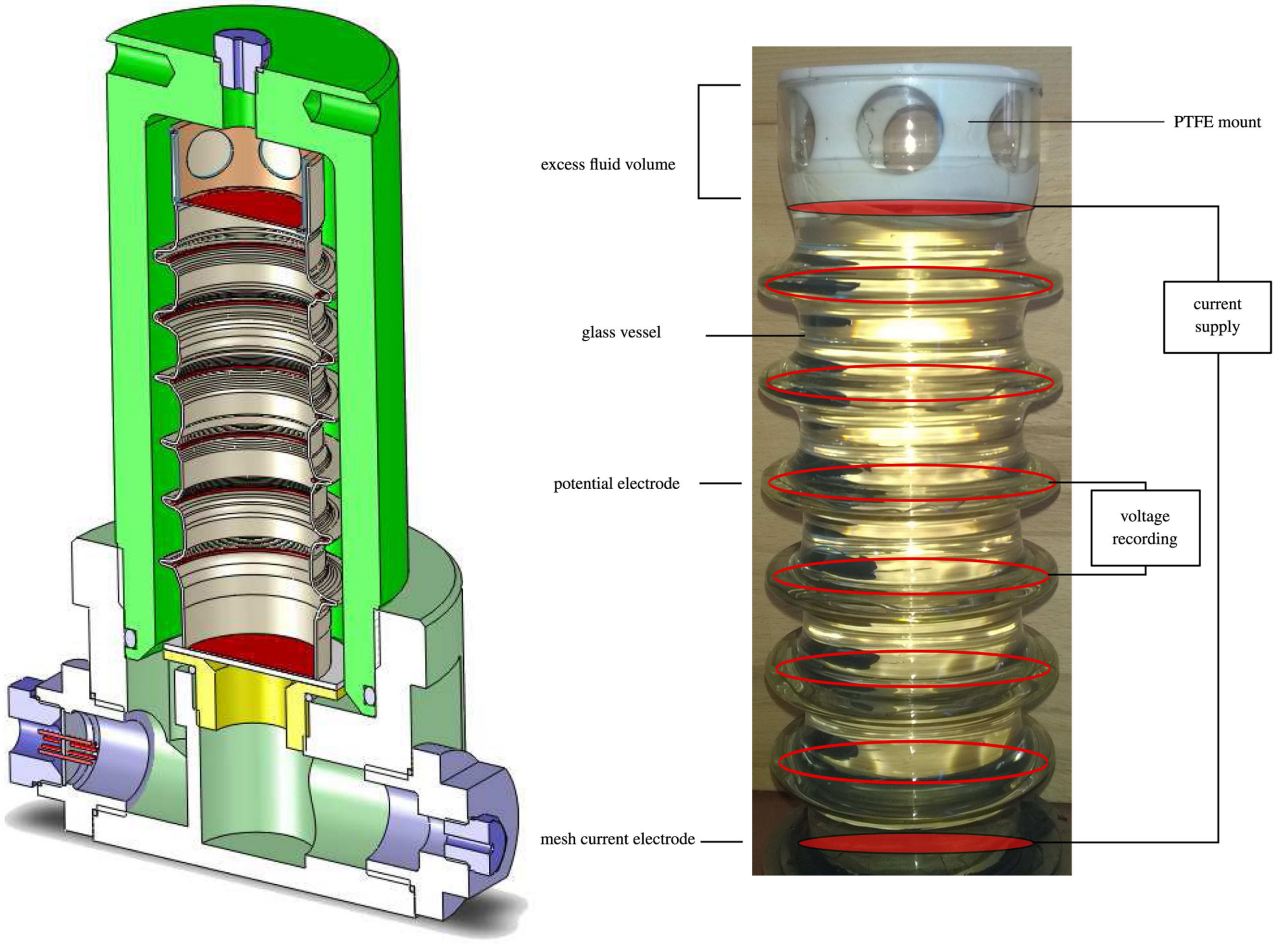

Figure 7. The autoclave with the measuring cell (left) and the glass cell with the electrodes indicated (right). PTFE is short for polytetrafluoroethylene.

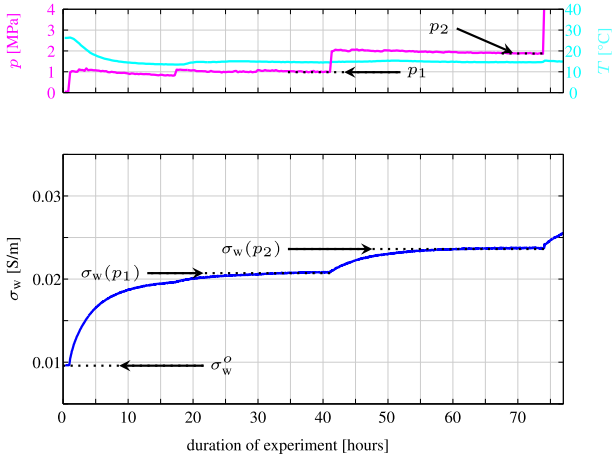

Figure 8. Eighty-five-hr example sequence of monitoring the conductivity σ_w for a 0.058 g L^{-1} (0.001 mol kg^{-1}) NaCl solution at 15 °C covering two pressure levels p_1 and p_2 (blue line, lower subplot). The corresponding pressure (magenta line) and temperature (cyan line) series are plotted in the top subplot. The pressure levels at 1 MPa (p_1) and 2 MPa (p_2) are indicated. The normalized conductivity at pressure level p_i may be obtained from $\sigma_w^{norm}(p_i) = \frac{\sigma_w(p_i)}{\sigma_w^o}$ (*cf.* eq. 22).

water is denser than CO_2-free pore water) or small temperature variations give rise to a very efficient free convection within the sample. Due to the convection-dominated equilibration no concentration gradients have been observed.

After closing the autoclave, the different pressure levels are adjusted by a CO_2 pump and a two-staged pressure regulating valve (see Fig. 8). The autoclave is placed in a hot air cabinet to reach and maintain the set temperature during the experiment in a small range of fluctuation. To reach equilibrium solubility of CO_2 in and equilibrium conductivity of the specific brine solution, the operating conditions are applied to the system for several hours, even up to days at low salinities and temperatures (see Fig. 8). At the end of the experiment, the pressure inside of the autoclave was reduced in a controlled manner.

3.4 Experimental agenda

Several aspects were systematically investigated in detail using the setup described above (*cf.* red circles in Fig. 2 for investigated pressure/temperature combinations):

(i) Pressure dependence of conductivity: a strong dependence on pressure has to be expected due to the dependence of CO_2 solubility on pressure (*cf.* Fig. 3) and former observations from Börner *et al.* (2013). Therefore, the conductivity of all aqueous solutions has been investigated at numerous pressure levels starting with 1 MPa up to 30 MPa at constant temperature and salinity.

(ii) Temperature dependence of conductivity: besides the strong temperature dependence of brine solutions, which may easily be compensated (see e.g. Worthington *et al.* 1990), an additional temperature dependence has to be expected due to the reduced CO_2 solubility at elevated temperatures (*cf.* Fig. 3). This effect cannot be eliminated computationally by a temperature correction. Consequently, we investigated one aqueous solution at four temperatures ranging from 8 to 80 °C. All other solutions were tested at two temperatures (15 and 80 °C).

(iii) Salinity dependence of conductivity: the salinity of the initial solution strongly influences the impact of CO_2 on conductivity (see Börner *et al.* 2013) and is a basic ingredient for the solution conductivity (*cf.* eq. 12). Based on the results from Börner *et al.* (2013) we investigated sodium chloride solutions with salinities ranging from 0.006 g L^{-1} to 57.27 g L^{-1} (equivalent to 0.0001–1 mol kg^{-1}).

(iv) Ion species dependence of conductivity: the interaction between aqueous species may be highly individual. We therefore tested the response of 0.01 mol kg^{-1} solutions of several salts (NaCl, KCl, $MgSO_4$, $MgCl_2$) at 15 °C, since these conditions appeared most indicative in the case of sodium chloride. The investigated ion species exhibit different cation and anion species and different charge numbers of the cations and anions.

Overall the resulting data set covers 148 equilibrium conditions for 135 pressure–temperature–salinity–species combinations. To check reliability and precision, several experiments have been repeated yielding maximum deviations of 3 per cent in pore water conductivity. The observed slight variations in the equilibrium conductivities may originate from small differences in the environmental conditions or small variations in the initial solution salinity (which is especially sensitive at very low concentrations).

The independence of the equilibrium conductivity from the experimental procedure was tested by comparing the results with experiments where the solution was equilibrated after a pressure decrease rather than a pressure increase. In this case, dissolved CO_2 obviously has to outgas from the solution rather than dissolve to reach equilibrium at constant temperature. For this testing, no hysteresis behaviour was observed – the equilibrium conductivities match within 1.9 per cent.

4 RESULTS

4.1 Laboratory data set

The resulting data set is plotted in Fig. 9. The conductivity contrast σ_w^{norm} is plotted for several salinities (one salinity per subfigure) and temperatures (from 8 °C in blue to 80 °C in red) versus pressure. The data at a (supposed) salinity of 0.006 g L^{-1} are not plotted, since a reliable determination of the salt content was not possible (*cf.* Fig. 5). Mainly depending on salinity, two regimes and a transition zone may be distinguished:

(i) For small salinities (below 0.6 g L^{-1}), we observe an increase in the electrical pore water conductivity for all temperatures when pressure increases (see subplots a and b in Fig. 9), which generally agrees with the behaviour of CO_2 solubility (*cf.* Fig. 3). This is the expected behaviour, since the additional ions originating from the dissociation of carbonic acid contribute to the solution conductivity. An additional conductivity contribution appears due to the new charged species in the solution (*cf.* eq. 14). Pore water conductivity may increase by more than factor 3 for low salinities and low temperatures. We call this behaviour the ‘low-salinity regime’.

(ii) When slightly higher salinities are considered this effect is diminished (Fig. 9c at 80 °C). This is still the expected behaviour, since the contribution of CO_2 has a smaller impact on the total solution conductivity when the initial pore water conductivity is higher. This transition between the two regimes occurs—depending on temperature—around 0.6 g L^{-1} NaCl.

(iii) For solutions with high NaCl content of 5.8 g L^{-1} or higher, the data set reveals an unexpected behaviour. No conductivity increase may be observed (subplots d and e in Fig. 9). The effect is even overcompensated and we observe a conductivity decrease by

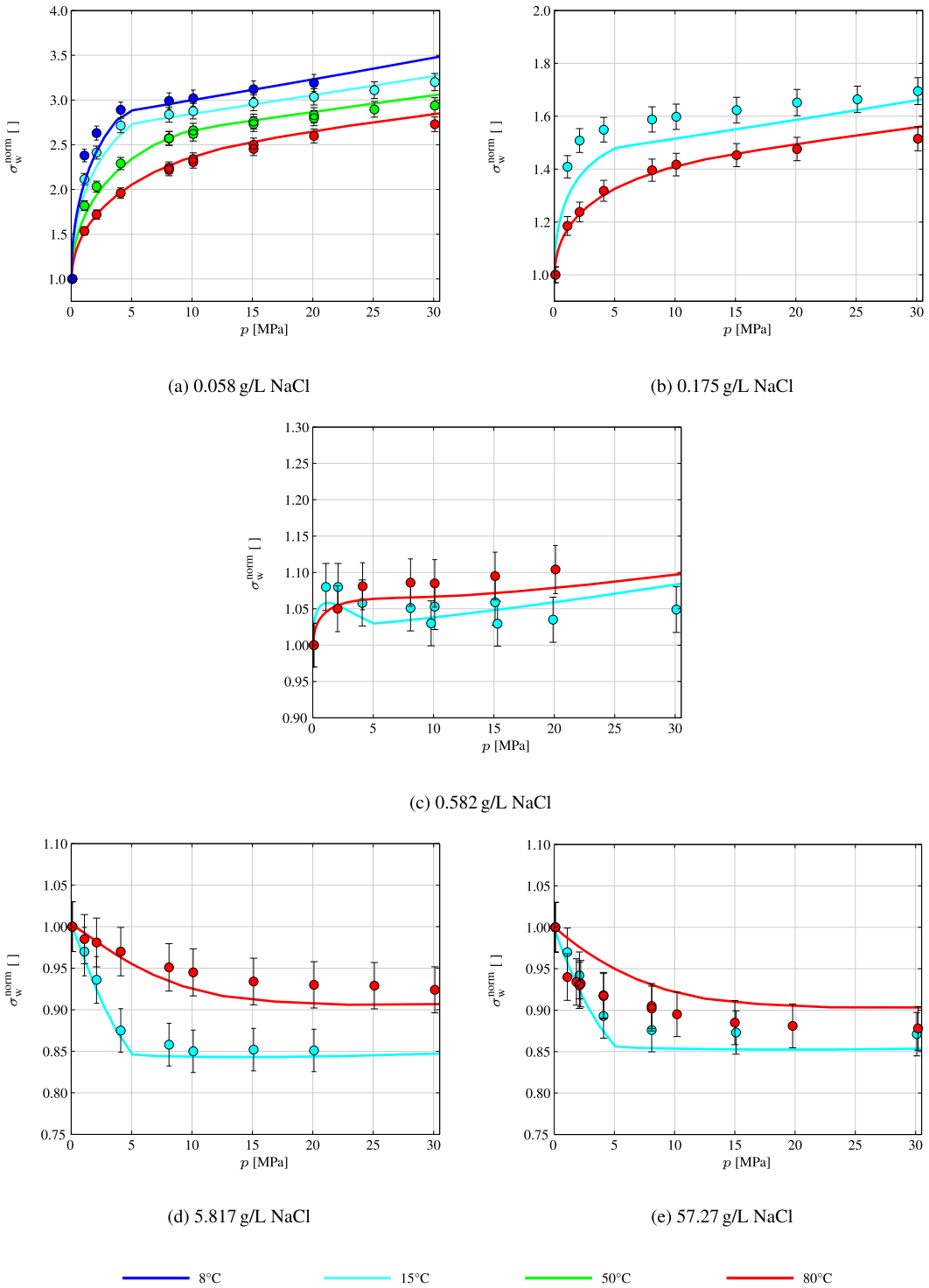

(a) 0.058 g/L NaCl

(b) 0.175 g/L NaCl

(c) 0.582 g/L NaCl

(d) 5.817 g/L NaCl

(e) 57.27 g/L NaCl

Figure 9. Measured conductivity contrast due to CO_2 dissolution and dissociation for five salinities (dots denote data, colours denote temperature) versus pressure. Three per cent error bars are plotted in black. Straight lines represent the model prediction (*cf.* Section 4.2). The sharp bend at subcritical temperatures is caused by the phase transition from gaseous to liquid state (*cf.* Figs 2 and 4 and eq. 10).

up to 15 per cent. This is smaller than the maximum effect in the low-salinity regime but still significant. We call this the 'high-salinity regime'.

Our high-salinity regime data are in good agreement with observations from Fleury & Deschamps (2008), who carried out injection experiments with porous alumina ceramics and CO_2-bearing NaCl solutions (not at thermodynamic equilibrium) at high salt concentrations ranging from 20–160 g L^{-1}. This means, that solution conductivity decreases although additional ions are provided and a new conductivity contribution is generated. The explanation for this behaviour is that—depending on salinity and the

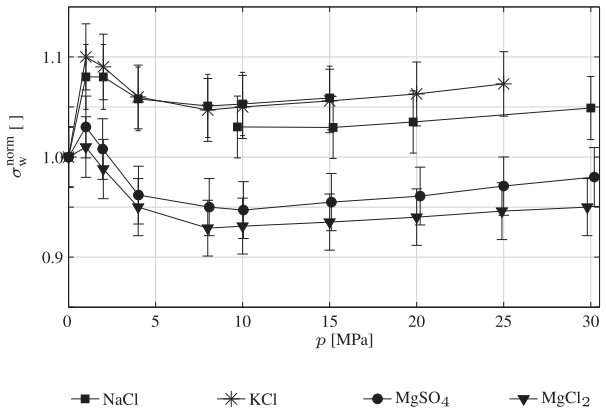

Figure 10. Comparison between several salts for 0.01 mol kg^{-1} solutions at 15 °C. Three per cent error bars are indicated. Note that the black lines are just for visual guidance.

environmental conditions—either the additional conductivity contribution from dissociated CO_2 or the growing limitations for the mobility of the salt component dominate the solution conductivity. To explain our observations in more detail we present a semi-analytical model in the following section, which is based on eq. (16).

Since the concentration around 0.58 g L^{-1} NaCl (0.01 mol kg^{-1}) at 15 °C is in the transition between the low- and high-salinity regime, it is most sensitive to the presence of both processes. To check whether the two regimes exist for salts with, for example, bivalent and or complex ions as well, potassium chloride, magnesium sulphate and magnesium chloride solutions were investigated at a molality of 0.01 mol kg^{-1} and at 15 °C (*cf.* Table 2). The results for all salts are plotted together with the data for sodium chloride already shown in Fig. 10. It becomes obvious that the general behaviour of a conductivity increase at low pressures changing into a conductivity decrease at high pressures is present for all salt species. KCl and NaCl show almost identical effects. Also the salts forming bivalent ions behave in a similar manner. Although the model derived in the following section is valid only for NaCl solutions, analogue formulations can probably be found for other salts and salt mixtures.

4.2 Model of the electrical pore water conductivity

A model approach for the electrical conductivity of a NaCl solution with CO_2 in thermodynamic equilibrium is now derived to explain and predict the observed two-regime behaviour. The model is based on eq. (16) and considers two conductivity contributions ($k = 2$), one originating from NaCl and one originating from CO_2. We therefore express the electrical conductivity of a NaCl solution bearing dissolved and dissociated CO_2 as

$$\sigma_w = \Lambda_{NaCl}\gamma_{NaCl}c_{NaCl} + \Lambda_{CO_2}\gamma_{CO_2}c_{CO_{2(dis)}} \tag{20}$$

with molar conductivities Λ_{NaCl} and Λ_{CO_2} and activity coefficients γ_{NaCl} and γ_{CO_2}. The activity coefficients γ_{NaCl} and γ_{CO_2} should not be interpreted as activity coefficients in the narrower chemical sense of the word. All processes contributing to the impediment of conduction are joined in these quantities. As described in Section 2.1 we solely consider the first stage of dissociation. CO_2 acts with a single conductivity contribution, therefore. Note that, while b_{NaCl} is constant throughout one experiment, the concentration c_{NaCl} is pressure and temperature dependent (*cf.* eq. 5).

At the beginning of each experiment no CO_2 is dissolved in the saline solution ($c_{CO_2} = c_{CO_{2(dis)}} = 0$). The conductivity of the initial solution σ_w^o may therefore be written as

$$\sigma_w^o = \Lambda_{NaCl}\gamma_{NaCl}^o c_{NaCl}, \tag{21}$$

where γ_{NaCl}^o is the activity coefficient of the pure NaCl solution. The molar conductivity of NaCl at infinite dilution Λ_{NaCl} equals to 0.216 S L m^{-1} g^{-1} at 25 °C (Hamann & Vielstich 1998). We assume that NaCl is fully dissociated ($\alpha_{NaCl} = 1$, $c_{NaCl} = c_{NaCl(dis)}$). We obtain the normalized electrical conductivity σ_w^{norm}, which is equivalent to the conductivity contrast measured in the experiments (see Fig. 8), of a pore water influenced by dissolving and dissociating CO_2 by dividing eq. (20) by eq. (21):

$$\sigma_w^{norm} = \frac{\sigma_w}{\sigma_w^o} = \frac{\left(\Lambda_{NaCl}\gamma_{NaCl}c_{NaCl} + \Lambda_{CO_2}\gamma_{CO_2}c_{CO_{2(dis)}}\right)}{\Lambda_{NaCl}\gamma_{NaCl}^o c_{NaCl}}. \tag{22}$$

Several quantities in this formulation are known, such as c_{NaCl}, Λ_{NaCl} and γ_{NaCl}^o (*cf.* Fig. 3). Others may be computed with models from the literature, such as α and c_{CO_2} and therefore also $c_{CO_{2(dis)}}$ (*cf.* eq. 10 and Section 2.1). Remaining unknowns are Λ_{CO_2} with its temperature dependence and the activity coefficients γ_{NaCl} and γ_{CO_2}.

Many authors have investigated activity coefficients in mixed electrolyte solutions. Based on the principles developed by Harned (1962), which where adapted, refined and enhanced by many authors (e.g. Badarayani & Kumar 2001; Robinson & Stokes 2002), we choose the following formulation for the activity coefficients (again in the logarithmized form):

$$\ln(\gamma_{NaCl}) = \ln(\gamma_{NaCl}^o) - g_{12}c_{CO_2} - h_{12}c_{CO_2}^2 \tag{23}$$

$$\ln(\gamma_{CO_2}) = \ln(\gamma_{CO_2}^o) - g_{21}c_{NaCl} - h_{21}c_{NaCl}^2. \tag{24}$$

Hereby, the activity coefficient of component i is built from γ_i^o (the activity coefficient of a solution containing i only) and additional terms describing the influence of the other component on the activity coefficient of i. The interaction parameters g_{12}, g_{21}, h_{12} and h_{21} are unknown. It is also important to point out that *all* dissolved CO_2 (c_{CO_2}) contributes to γ_{NaCl}, not only the dissociated portion $c_{CO_{2(dis)}}$. This is in accordance with observations from the literature, that also neutral molecules such as the solvent itself or not dissociated gases interact with the charged species and may influence their activity (e.g. Hamann & Vielstich 1998). We use the Debye–Hückel activity coefficient to describe $\gamma_{CO_2}^o$ (*cf.* eq. 17). Note that the ionic strength I in this case only includes the species of the first stage of the dissociation of CO_2 (*cf.* eq. 6). The dielectric permittivity ϵ depends on temperature and is computed with the model from Fernández *et al.* (1995). The pressure dependence of ϵ is negligible in the pressure and temperature range considered in this study (Uematsu & Franck 1980).

The remaining unknowns are determined by a regularized, iterative least-squares fitting (see Table 3). A data weighting is included. The data for 0.058, 0.582 and 57.27 g L^{-1} were included in the inversion. This comes up to approximately 75 per cent of the whole data set. The remaining 25 per cent of the data (0.006, 0.175 and 5.817 g L^{-1}) served as control group. In analogy to Worthington *et al.* (1990) the temperature dependence of Λ_{CO_2} is assumed to be linear with an unknown proportionality factor. Based on the observations a slight linear dependence on pressure is introduced for g_{12}, which is not part of the inversion and might be due to the assumptions of Ostwald's law (eq. 9) being violated at high salinities.

The resulting model predictions are plotted as continuous lines in the subplots of Fig. 9. The model predictions generally agree very

Table 3. Parameters of the final model derived by least-squares inversion. See also eqs (22)–(24).

Parameter	Value
Λ_{CO_2}	$6.285 \times 10^{-1} \cdot \left(\frac{\frac{T}{T_o}-242.6}{55.59}\right)$ S L m^{-1} g^{-1} [a]
g_{12}	$2.933 \times 10^{-2} \cdot \left(1 - 7 \times 10^{-4} \frac{p}{p_o}\right)$ S L g^{-1} [b]
g_{21}	2.623×10^{-4} L g^{-1}
h_{12}	1.066×10^{-5} L^2 g^{-2}
h_{21}	2.065×10^{-3} L^2 g^{-2}

[a] With $T_o = 1$ K.
[b] With $p_o = 1$ bar.

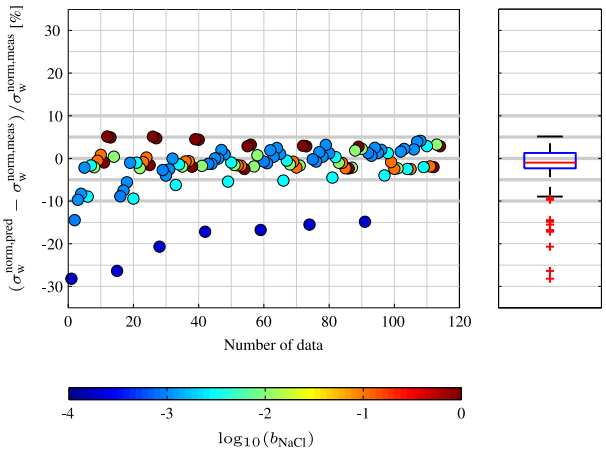

Figure 11. Deviation between measured data and prediction from the semi-analytical model (*cf.* eqs 22–24). The red line in the boxplot refers to the median. The upper and lower boundary of the blue box relate to the 25 per cent and 75 per cent quartile, respectively. Ninety per cent of the data lay within the range of the black whiskers. Larger deviations are marked by red crosses.

well with the whole data set. The low- and high-salinity regimes are covered and also the complex transition is represented correctly. For our data set, the linear temperature dependence appears to be sufficient. The deviation between predicted and measured data is addressed in Fig. 11. The left subplot of Fig. 11 shows the percentage deviation of predicted from measured data. Colours denote salinity. The right-hand side subplot contains a boxplot of these deviations. These plots show that 50 per cent of the whole data set are explained with a deviation between −2.3 per cent and 1.3 per cent by our model (see extension of the blue box in Fig. 11, right). At the same time 90 per cent of the data set are explained with a deviation between −8.9 per cent and 5.2 per cent (see extension of the whiskers in Fig. 11, right). Large deviations mainly occur at very low salinities (*cf.* blue circles in Fig. 11). This is due to the unreliable salinity assignment.

4.3 Application on pore water conductivity

The model described in the former section predicts our data very well and helps to understand the fundamental processes, which lead to the two-regime behaviour of conductivity. However, the application of the developed model requires the computation of many physico-chemical quantities and their dependence on pressure, temperature and salinity. This effort might not be feasible for the integration of our results into simulation studies or for monitoring applications. Therefore, we additionally provide a purely empirical formulation for the conductivity contrast σ_w^{norm}, which allows to

Table 4. Parameters of the empirical representation of conductivity contrast (*cf.* eq. 25).

Parameter	Value
q_1	2.65×10^{-1} g L^{-1}
q_2	-5.49×10^{-4} g L^{-1} K^{-1}
q_3	1.23×10^{-3} g L^{-1} MPa^{-1}
q_4	3.24×10^{0} MPa^{-1}
q_5	-7.74×10^{-3} K^{-1} MPa^{-1}
q_6	5.18×10^{-1}
q_7	-1.25×10^{-3} K^{-1}
q_8	3.28×10^{-1} MPa^{-1}

predict the *in situ* impact of CO_2 based on the presented data with information on formation salinity, temperature and pore pressure only:

$$\sigma_w^{norm} = 1 + \frac{q_1 + q_2 T + q_3 p}{c_{NaCl}} (1 - \exp[-(q_4 + q_5 T)p]) - (q_6 + q_7 T)(1 - \exp[-q_8 p]). \quad (25)$$

The salinity c_{NaCl} is in g L^{-1}, temperature is in K and pressure is in MPa. The parameters q_i are purely empirical and bear no distinct physical or chemical meaning. The general structure of this formulation includes two competing processes, which move towards an equilibrium for high pressures, and is based on the empirical adaptation of Archie's law given by Börner *et al.* (2013).

The parameters q_i are derived by an iterative least-squares inversion of the whole data set (except for the 0.006 g L^{-1} data). Their values are documented in Table 4. In analogy to the semi-analytical model we address the prediction quality of the empirical representation in Fig. 12. The empirical model explains our data even better than the physico-chemical one (eq. 22). For 50 per cent of the data, the prediction deviates within a range of −1.8 per cent to 2.1 per cent from the observations (see extension of the blue box in Fig. 12, right), for 94 per cent of the data the prediction lies within −4.5 per cent to 5.6 per cent (see extension of the whiskers in Fig. 11, right). For the same reasons, which have been discussed before, the prediction is worst for the very low salinity data.

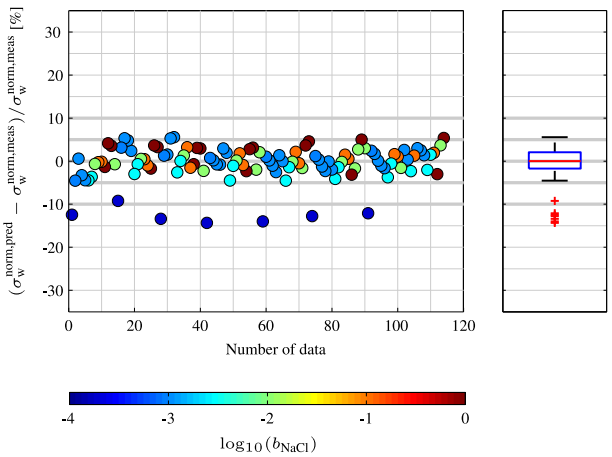

Figure 12. Deviation between measured data and the prediction from the empirical formulation (*cf.* eq. 25). The red line in the boxplot refers to the median. The upper and lower boundary of the blue box relate to the 25 per cent and 75 per cent quartile, respectively. Ninety-four per cent of the data lay within the range of the black whiskers. Larger deviations are marked by red crosses.

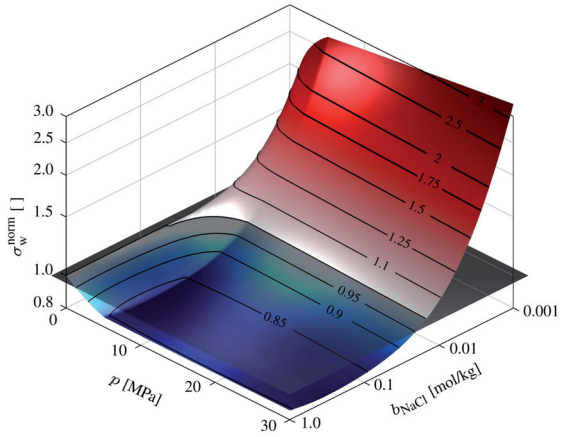

(a) 3D plot of conductivity contrast due to CO_2 dissolution and dissociation according to Equations 22 – 24 vs. pressure and salinity at 15°C.

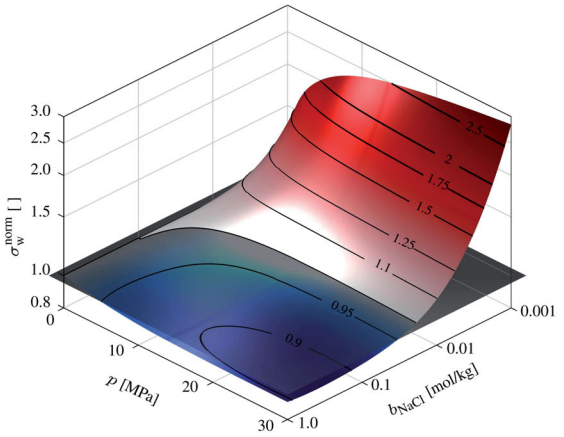

(b) 3D plot of conductivity contrast due to CO_2 dissolution and dissociation according to Equations 22 – 24 vs. pressure and salinity at 80°C.

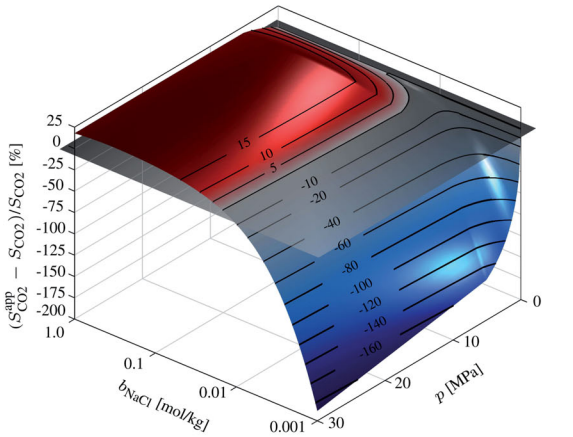

(c) Percentage error during estimation of CO_2 saturation S_{CO2}^{app} with Equation 1 from rock conductivity caused by neglecting the impact of CO_2 dissolution and dissociation on pore water conductivity vs. salinity and pressure at 15°C (in case of a clay-free reservoir).

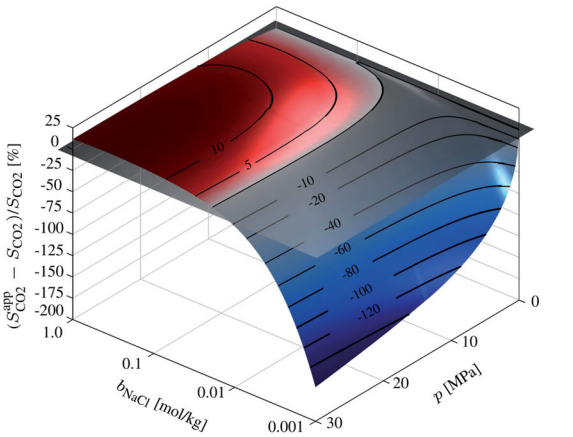

(d) Percentage error during estimation of CO_2 saturation S_{CO2}^{app} with Equation 1 from rock conductivity caused by neglecting the impact of CO_2 dissolution and dissociation on pore water conductivity vs. salinity and pressure at 80°C (in case of a clay-free reservoir).

Figure 13. 3-D plots of conductivity contrast (top) and potential balancing error (bottom) for demonstration of the necessity to take CO_2 dissolution and dissociation into account. The true CO_2 saturation S_{CO2} is 0.3 and the saturation exponent n is 2. The plane where no impact occurs ($\sigma_w^{norm} = 1$ in the top figures and $(S_{CO2}^{app} - S_{CO2})/S_{CO2} = 0$ per cent in the bottom figures) is shown in transparent grey.

5 DISCUSSION

The findings of the presented laboratory investigation have several implications for both synthetic studies and practical geophysics. First of all, they might have to be considered during monitoring of a CO_2 injection in deep saline aquifers (Börner *et al.* 2015). When electromagnetic methods are applied to monitor the CO_2 content ($S_{CO2} = 1 - S_w$; see eq. 1) in the pore space of a storage formation, changes in rock conductivity are associated with changes in water saturation, e.g., by exploiting Archie's law (see eq. 1; Archie 1942, holds for clay-free reservoirs). The effect of CO_2 dissolution on this balancing and its dependence on pressure and pore water salinity is demonstrated in Fig. 13 for a formation with a true CO_2 content of $S_{CO2} = 0.3$ and a saturation exponent equal to 2 at 15 °C and 80 °C. Figs 13(a) and (b) show the according normalized pore water conductivity (eq. 22) and Figs 13(c) and (d) show the percentage difference between the apparent CO_2 content S_{CO2}^{app} (where the change of σ_w has not been accounted for) and the true CO_2 content. In Figs 13(c) and (d), blue colours refer to an underestimation and red colours to an overestimation of CO_2 content.

Potential storage formations are usually located at considerable depth, where pore water salinity is high. For most CO_2 storage sites, the high-salinity regime has to be assumed, therefore. Consequently, when the conductivity decreasing impact of CO_2 on the pore water is not taken into account, the interpretation of changes in rock conductivity will yield an overestimated CO_2 saturation (see red colours in Figs 13 c and d). This systematic error might result in an erroneous balancing of the free CO_2 within the reservoir.

Another focus of monitoring applications is the safety of shallow ground water resources, which are essential for drinking water supply. A robust and effective surveillance of laterally wide spread areas may be realized with geophysical techniques. CO_2 migration into shallow ground water bodies would result in plumes of CO_2 loaded ground water. How such a plume appears in time-lapse electrical measurements strongly depends on the ion content of the ground water. Our study shows, that for clean fresh water aquifers the low-salinity regime applies and a conductive anomaly may be

expected. However, the transition towards the high-salinity regime already starts at rather moderate salinities (*cf.* Fig. 9c). When the aquifer's salinity is in that range, a very complex anomaly may be caused by the migrating CO_2. Small local or temporal changes in temperature, pressure, salinity or leakage rate can change the anomaly from a conductive to a resistive nature. As a worst case scenario, also a complete masking of the CO_2 leakage is possible. The environmental conditions and chemical properties of the target aquifer have to be investigated most carefully before an electrical monitoring is installed, therefore.

6 CONCLUSIONS

Our laboratory study shows that the reactive nature of CO_2 in all physical states significantly acts on the electrical conductivity of an aqueous salt solution. The physicochemical interaction appears in different manifestations depending mainly on the salinity of the solution but also on temperature and pressure. It could be shown that the complex behaviour including a low- and high-salinity regime originates in the conductivity increasing effect of CO_2 dissociation, which is opposed by the conductivity decreasing effect of reduced ion activity caused by the enhanced mutual impediment of all solutes.

We derive a semi-analytical formulation to predict these effects. To enable the implementation of our results in practice, we also provide an empirical relationship for the impact of CO_2 on pore water conductivity, which only requires the knowledge of temperature, pressure and salinity. Our findings are in accordance with the results from former studies. Though most of the experiments were carried out using NaCl solutions, exemplary series of measurements with other salts indicate that a qualitatively comparable behaviour may be expected for other salt solutes as well.

Applications of our results are the reliable interpretation of electrical rock conductivity in terms of CO_2 saturation and a detailed understanding of the complex electrical anomalies, which might occur during leakage detection. Further investigations should aim at testing mixed electrolytes containing several salt components. This is important, since mixtures do not necessarily act in the same way as single electrolytes. The interaction between the different salt ion species adds new degrees of freedom to the activity of all components. Furthermore, the knowledge about the interaction between the mobile phases now allows more detailed and specific investigations of the process of injection of CO_2 into water bearing porous media. A study on the spectral electrical properties of the three-phase system rock matrix/pore water/CO_2 at elevated pressure and temperature will follow the presented survey.

ACKNOWLEDGEMENTS

This work has been funded by the German Research Foundation (DFG) (grant numbers SP 356/12-1 and RE 1705/9-1). Additionally, Jana H. Börner thanks the Christiane Nüsslein-Volhard-Foundation for their support. Furthermore, the authors thank two anonymous reviewers for helping improve this manuscript.

REFERENCES

Archie, G.E., 1942. The electrical resistivity log as an aid in determining some reservoir characteristics, *Trans. Americ. Inst. Mineral. Met.,* **146**(146), 54–62.

Badarayani, R. & Kumar, A., 2001. A simple model for estimation of activity coefficients of salts in aqueous and nonaqueous solutions and their mixtures up to high temperatures, *Ind. Eng. Chem. Res.,* **40**(8), 1996–2003.

Binley, A., Cassiani, G., Middleton, R. & Winship, P., 2002. Vadose zone flow model parameterisation using cross-borehole radar and resistivity imaging, *J. Hydrol.,* **267,** 147–159.

Börner, J.H., Herdegen, V., Repke, J.-U. & Spitzer, K., 2013. The impact of CO_2 on the electrical properties of water bearing porous media - laboratory experiments with respect to carbon capture and storage, *Geophys. Prospect.,* **61,** 446–460.

Börner, J.H., Wang, F., Weißflog, J., Bär, M., Görz, I. & Spitzer, K., 2015. Multi-method virtual electromagnetic experiments for developing suitable monitoring designs: a fictitious CO_2 sequestration scenario in Northern Germany, *Geophys. Prospect.*, doi:10.1111/1365-2478.12299.

Bromley, L.A., 1973. Thermodynamic properties of strong electrolytes in aqueous solutions, *AIChE J.,* **19**(2), 313–320.

Davies, C., 1962. *Ion Association*, Butterworths.

Debye, P., 1923. On ions and their activity, *Chemisch Weekblad,* **20,** 562–568.

Debye, P. & Hückel, E., 1923a. On the theory of electrolytes. I. Freezing point, *Physikalische Zeitschrift,* **24,** 185–206.

Debye, P. & Hückel, E., 1923b. On the theory of electrolytes. II. Limiting law for electric conductivity, *Physikalische Zeitschrift,* **24,** 305–325.

Dell'Aversana, P., Carbonara, S., Vitale, S., Subhani, M. & Otiocha, J., 2011. Quantitative estimation of oil saturation from marine CSEM data: a case history, *First Break,* **29**(2), 53–62.

Duan, Z., Sun, R., Zhu, C. & Chou, I., 2006. An improved model for the calculation of CO_2 solubility in aqueous solutions containing Na^+, K^+, Ca^{2+}, Mg^{2+}, Cl^- and SO_4^{2-}, *Marine Chemistry,* **98,** 131–139.

Duan, Z., Hu, J., Li, D. & Mao, S., 2008. Densities of the CO_2–H_2O and CO_2–H_2O–NaCl systems up to 647 K and 100 MPa, *Energy & Fuels,* **22,** 1666–1674.

Fernández, D., Goodwin, A.R.H. & Sengers, J.M.H., 1995. Measurements of the relative permittivity of liquid water at frequencies in the range of 0.1 to 10 kHz and at temperatures between 273.1 and 373.2 K at ambient pressure, *Int. J. Thermophys.,* **16**(4), 929–955.

Fleury, M. & Deschamps, H., 2008. Electrical conductivity and viscosity of aqueous NaCl solutions with dissolved CO_2, *Journal of Chemical and Engineering Data,* **53,** 2505–2509.

Glover, P.W.J., 2010. A generalized Archie's law for n phases, *Geophysics,* **75,** E247–E265.

Guggenheim, E.A. & Turgeon, J.C., 1955. Specific interaction of ions, *Trans. Faraday Soc.,* **51,** 747–761.

Hamann, C.H. & Vielstich, W., 1998. *Elektrochemie*, Wiley-VCH.

Harned, H., 1962. A rule for the calculation of the activity coefficients of salts in organic solvent-water mixtures, *J. Phys. Chem.,* **66**(4), 589–591.

Helgeson, H., 1969. Thermodynamics of hydrothermal systems at elevated temperatures and pressures, *Am. J. Sci.,* **267,** 729–804.

Hitchon, B., 1996. *Aquifer Disposal of Carbon Dioxide*, Geoscience Publishing Ltd.

IPCC, 2005. *IPCC Special Report on Carbon Dioxide Capture and Storage*, Prepared by Working Group III of the Intergovernmental Panel on Climate Change, Cambridge University Press.

Kiessling, D., Schmidt-Hattenberger, C., Schuett, H., Schilling, F., Krueger, K., Schoebel, A., Danckwardt, E. & Kummerow, J., 2010. Geoelectrical methods for monitoring geological CO_2 storage: first results from cross-hole and surface—downhole measurements from the CO_2SINK test site at Ketzin (Germany), *International Journal of Greenhouse Gas Control,* **4,** 816–826.

Kummerow, J. & Spangenberg, E., 2011. Experimental evaluation of the impact of the interactions of CO_2-SO_2, brine, and reservoir rock on petrophysical properties: a case study from the Ketzin test site, Germany, *Geochem. Geophys. Geosyst.,* **12**(5), doi:10.1029/2010GC003469.

Kunkel, R., Hannappel, S., Voigt, H.-J. & Wendland, F., 2002. Die natürliche Grundwasserbeschaffenheit ausgewählter hydrostratigrafischer Einheiten in Deutschland, Tech. rep., Forschungszentrum Jülich, HYDOR Consult GmbH, BTU Cottbus.

Li, D. & Duan, Z., 2007. The speciation equilibrium coupling with phase equilibrium in the H_2O-CO_2-NaCl system from 0 to 250°C, from 0 to 1000 bar, and from 0 to 5 molality of NaCl, *Chem. Geol.,* **244**, 730–751.

Marini, L., 2007. Geological sequestration of carbon dioxide - thermodynamics, kinetics and reaction path modelling, in *Developments in Geochemistry*, Vol. 11, 1st edn, Elsevier.

Meju, M.A., 2002. Geoelectromagnetic exploration for natural resources: Models, case studies and challenges, *Surv. Geophys.,* **23**(2–3), 133–206.

Millero, F., Huang, F., Graham, T. & Pierrot, D., 2007. The dissociation of carbonic acid in NaCl solutions as a function of concentration and temperature, *Geochim. Cosmochim. Acta,* **71,** 46–55.

Möller, P. *et al.*, 1997. Paleofluids and recent fluids in the upper continental crust: results from the German continental deep drilling program (KTB), *J. geophys. Res.,* **102**(B8), 18 233–18 254.

Müller-Huber, E., Schön, J. & Börner, F., 2015. The effect of a variable pore radius on formation resistivity factor, *J. Appl. Geophys.,* **116,** 173–179.

Pitzer, K., 1991. *Activity Coefficients in Electrolyte Solutions*, 2nd edn, CRC Press.

Robinson, R. & Stokes, R., 2002. *Electrolyte Solutions*, 2nd edn, Dover.

Span, R. & Wagner, W., 1996. A new equation of state for carbon dioxide covering the fluid region from the triple-point temperature to 1100 K at pressures up to 800 MPa, *J. Phys. Chem. Ref. Data,* **25**(6), 1509–1596.

Uematsu, M. & Franck, E.U., 1980. Static dielectric constant of water and steam, *J. Phys. Chem. Ref. Data,* **9**(4), 1291–1306.

Vilamajó, E., Queralt, P., Ledo, J. & Marcuello, A., 2013. Feasibility of monitoring the Hontomín (Burgos Spain) CO_2 storage site using deep EM source, *Surv. Geophys.,* **34,** 441–461.

Vinegar, H.J. & Waxman, M.H., 1984. Induced polarization of shaly sands, *Geophysics,* **49**(8), 1267–1287.

Waxman, M.H. & Smits, L.J.M., 1968. Electrical conductivities in oil-bearing shaly sands, *Society of Petroleum Engineers Journal,* **8,** 107–122.

Wigand, M., Carey, J., Schütt, H., Spangenberg, E. & Erzinger, J., 2008. Geochemical effects of CO_2 sequestration in sandstones under simulated in situ conditions of deep saline aquifers, *Applied Geochemistry,* **23,** 2735–2745.

Worthington, A.E., Hedges, J.H. & Pallatt, N., 1990. SCA guidelines for sample preparation and porosity measurement of electrical resistivity samples–part I, *The Log Analyst,* **31,** 20–28.

Yardley, B., Manning, C. & Garven, G., 2011. *Frontiers in Geofluids*, Wiley.